Collisional-Radiative, Atomic Physics, and Radiation-Hydrodynamics Simulations of Aluminum and Silicon Targets Heated by the KALIF Proton Beam

J.J. MacFarlane, P. Wang, H.-K. Chung, J.F. Santarius

December 1996

UWFDM-1038

.

FUSION TECHNOLOGY INSTITUTE

UNIVERSITY OF WISCONSIN

MADISON WISCONSIN

Collisional-Radiative, Atomic Physics, and Radiation-Hydrodynamics Simulations of Aluminum and Silicon Targets Heated by the KALIF Proton Beam

J. J. MacFarlane, P. Wang, H.-K. Chung, and J. F. Santarius

Fusion Technology Institute
University of Wisconsin-Madison
1500 Engineering Drive
Madison, WI 53706

December 1996

UWFDM-1038

Contents

1. Introduction

The purpose of this report is to describe theoretical and computational work performed during the 1996 calendar year in support of the FZK KALIF program. This work, summarized in Table 1.1, has been concentrated primarily in two areas. First, we have performed radiation-hydrodynamics, atomic physics, and collisional-radiative simulations of KALIF proton beam-target interaction experiments. The purpose is to both assist in the interpretation of aluminum K_α spectra obtained in KALIF applied-B diode experiments, and to make predictions for K_α spectra emitted from silicon targets. Silicon has been discussed as a possible target material in upcoming KALIF experiments. This work is discussed in Section 2.

Second, we have made several improvements to our collisional-radiative code NLTERT. This includes the addition of a continuum lowering model based on the occupation probability method of Hummer and Mihalas [1]. In addition, the code was modified to solve *time-dependent* multilevel atomic rate equations. This allows one to more accurately simulate the ionization dynamics and spectra of low-to-moderate density plasmas. Examples include low-density ion source plasmas used to generate intense ion beams, and moderate-density plasmas through which intense ion beams can be transported.

Also during 1996, we participated in the first Non-LTE Kinetics Workshop in Gaithersburg, MD. At this workshop, researchers from a variety of laboratories and universities in Europe and the United States gathered to compare collisional-radiative computer simulation results for a number of benchmark problems. Workshops of this type are extremely valuable because they help identify strengths and weaknesses in simulation codes, as well as the sensitivity of results to modeling methods and assumptions. Several results from our calculations for this workshop are presented in Section 2. (Rules of the workshop, however, do not permit us to present results from other codes.) The workshop was particularly relevant to our work this year with FZK because it presented an opportunity to benchmark the newly-implemented time-dependent collisional-radiative model and the continuum lowering algorithm.

Table 1.1. Tasks for 1996

1. Analyze X-ray spectra obtained in KALIF proton beam experiments.
   (a) Compute atomic cross section data for target materials used in KALIF experiments.
   (b) Perform collisional-radiative equilibrium (CRE) calculations to predict K_α spectra.
2. Upgrade CRE code (NLTERT) to include continuum lowering effects using occupation probability model.
3. Modify CRE code to solve time-dependent rate equations for analyzing ionization dynamics of moderate-density plasmas.
4. Document results in Final Report to FZK. Supply FZK with updated NLTERT code.

2. Numerical Simulation of K_α Spectra Emitted by Al and Si Targets

In this section, we present results from radiation-hydrodynamics, collisional-radiative, and atomic physics calculations of Si and Al targets irradiated by an intense proton beam generated by the KALIF pulse powered device. Results for Al targets irradiated in KALIF applied-B diode experiments were discussed in detail in our interim 1996 report [2]. Here, we present new results for Si targets, and make several comparisons with the Al results. In particular, we examine the temperatures achieved in the target, the magnitude of the K_α flux from the Al and Si, and the target ionization and resultant space-dependent K_α satellite spectra.

2.1. Proton Beam Parameters

Since the spectrometer views an area of the target which comprises a range of temperature and beam intensity, both the space and time dependence of the proton beam across the target must be accounted for. This spatial integration effect could be mitigated in future experiments if targets could be fabricated in which a particular material (for example, Si) saw only the most intense "central" portion of the proton beam. This would require a small circular region with a radius $\lesssim$ the spot size of the beam.

A detailed description of the time- and space-dependent beam properties has been presented in Ref. [2], and only a brief summary is presented here. We assume a Gaussian beam profile in describing the space dependence. The current density distribution function is

$$f(r) = \frac{1}{\pi R_0^2}\, e^{-(r/R_0)^2}\,, \tag{2.1}$$

where r is the distance from the center of the beam (assumed to be cylindrically symmetric), and R_0 is a constant which is related to the measured beam diameter by:

$$R_0 = \frac{FWHM}{2(\ln 2)^{1/2}}\,, \tag{2.2}$$

where $FWHM$ is the full width of the beam at half maximum. In our simulations we use $R_0 = 0.37$ cm, which gives a $FWHM$ of 0.62 cm.

In practice, the spatial dependence of the beam is accounted for in the simulations by dividing the beam profile radially into 4 separate regions. For each region a 1-D radiation-hydrodynamics simulation is performed using BUCKY-1 [3] to predict the depth-dependent

plasma temperature and density, and ion beam kinetic energy (voltage) and current density. Beam parameters used in each region are given in Ref. [2].

The time dependence of the beam used in our simulations is given in Figure 2.1. This represents the peak current density (in space), so that the current density for region k is:

$$J(r_{\min,k} < r < r_{\max,k}; t) = J_{\rm peak}(t) \cdot C_k \,, \tag{2.3}$$

where C_k is a constant. (The values of C_k are tabulated in the last column of Table 2.1 of Ref. [2].)

2.2. Simulation Results

For each of the 4 spatial regions (representing areas on the target plane being irradiated at different beam intensities), 1-D radiation-hydrodynamics simulations were performed. To obtain time-integrated K_α satellite spectra, output from the hydrodynamics code at 10 ns intervals was post-processed using the NLTERT (CRE) code. The CRE K_α spectra were then post-processed to: (1) perform the time-integration; (2) include the instrumental spectral broadening ($\lambda/\Delta\lambda = 1000$); and (3) perform the space integration.

Simulations were performed for a 6 μm-thick Si target ($\rho\Delta L = 14.0$ mg/cm^2). Figure 2.2 shows the time-dependent mean temperature in each of the four regions ($A \rightarrow$ center of beam; see Fig. 2 of Ref. [2]). For comparison, the temperatures from the 6 μm Al simulation are shown as dashed curves. The peak temperature is predicted to be approximately $T = 30$ eV at 60 ns. However, it is expected that the contribution to the measured K_α spectra at times $\gtrsim 60$ ns is very small because the decrease in voltage at late times leads to lower proton-impact ionization cross sections and significantly weaker K_α line intensities. Figure 2.2 shows that for each of the regions, the Si temperature begins to exceed the corresponding Al temperature when T rises above approximately 6 eV. This may be due to Si having a greater number of free electrons (4 M-shell electrons available to liberate versus 3 for Al), which leads to a higher stopping power.

K_α satellite emission spectra for the Si target are shown in Figures 2.3-2.5 for Regions A, B, and C. Spectra are shown at 10 ns intervals for simulation times up through 70 ns. Note the change in the flux scale at the different times. Also note that these spectra do not include instrumental broadening.

In Region A, it is seen that by 30 ns the dominant emission has shifted from the "cold" K_α feature ($\lambda = 7.12$ Å) to O-like Si. Also, the intensity drops significantly due to

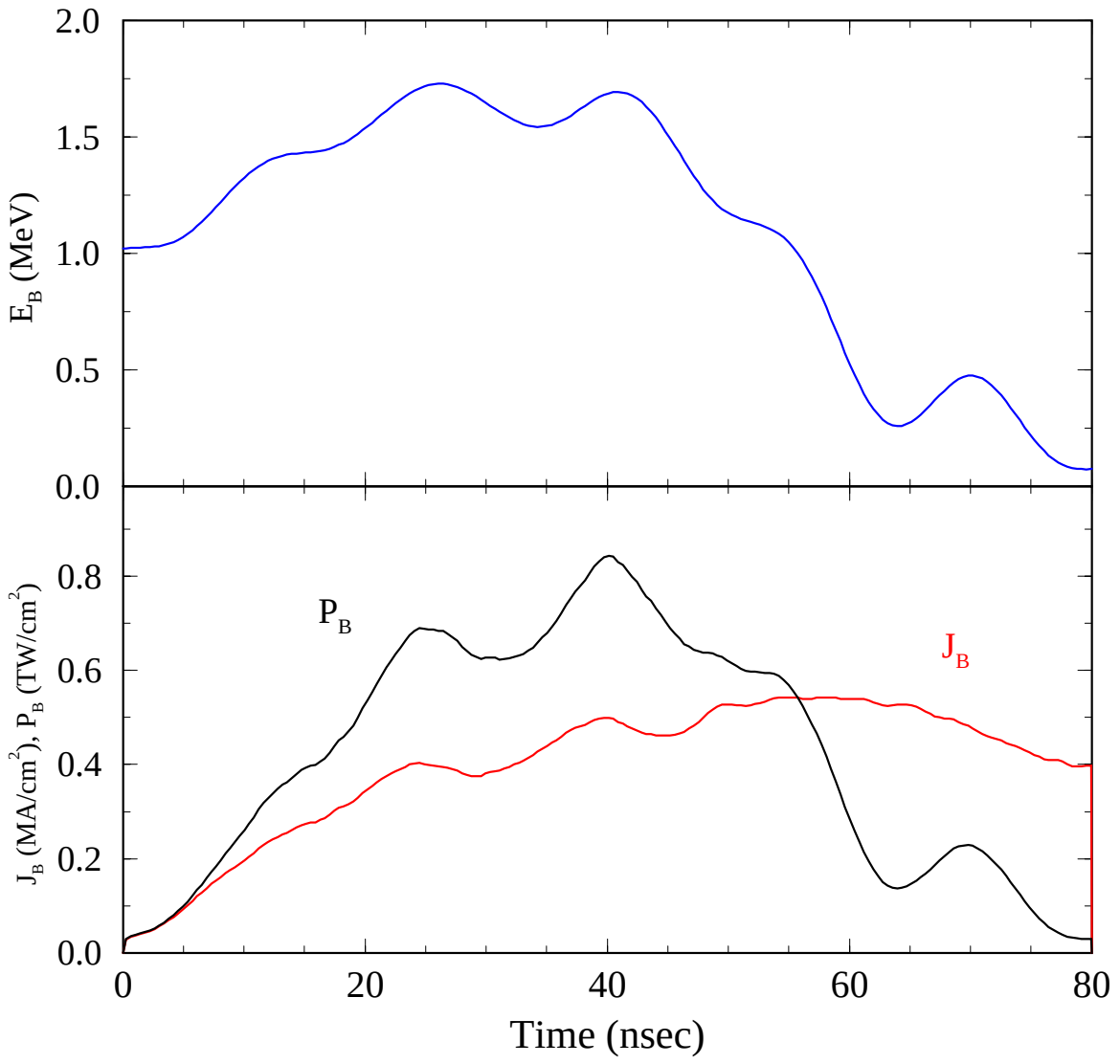

Figure 2.1. Time-dependent beam voltage, current density, and power density used in K_α target simulations. The current density shown corresponds to the (spatial) peak, $J_{\text{peak}}(t)$, used in Eq. (2.3).

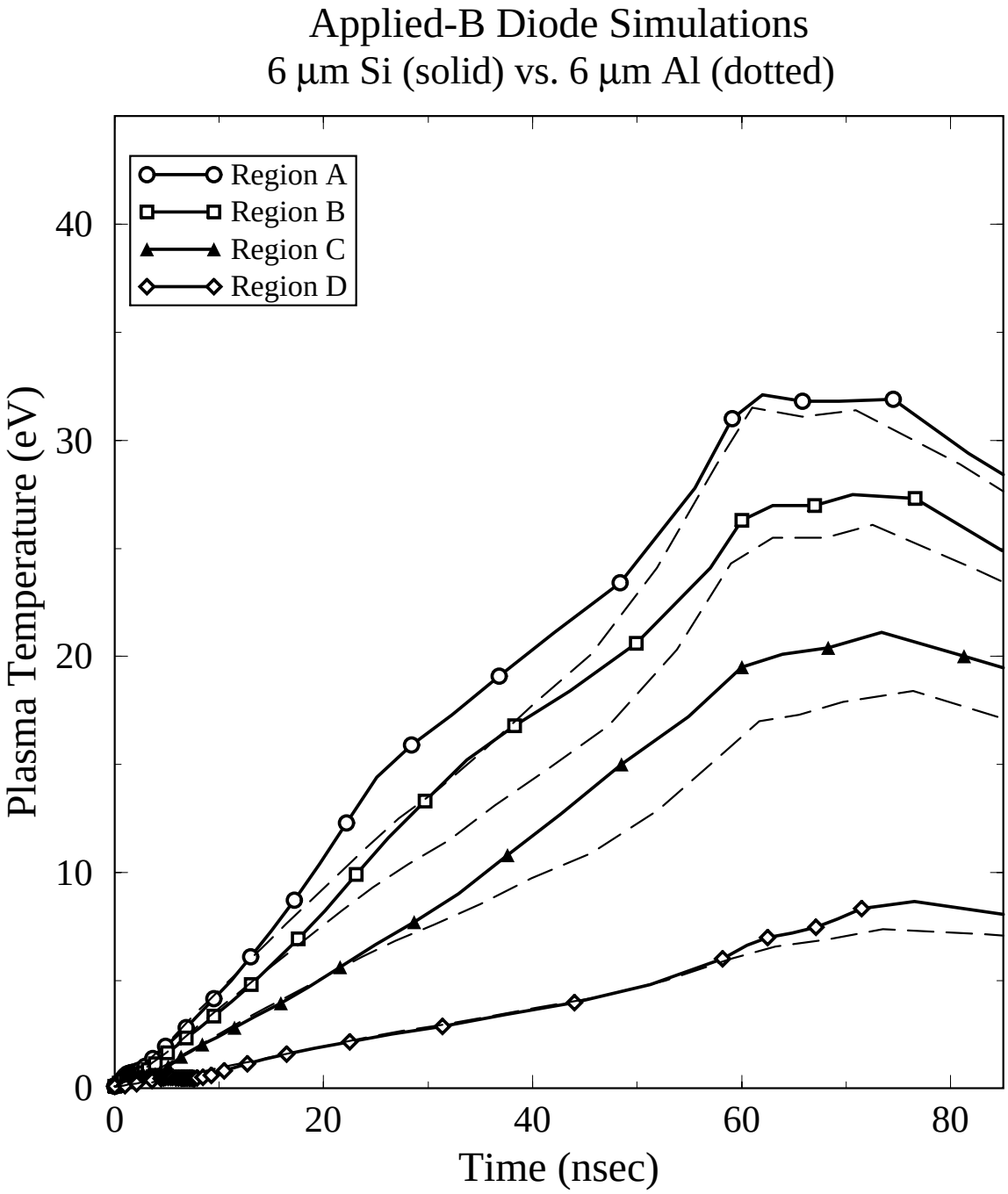

Figure 2.2. Calculated time evolution of mean plasma temperature in each spatial region (A = beam center) for a 6 μm Si target (solid curves) and a 6 μm Al target (dashed curves).

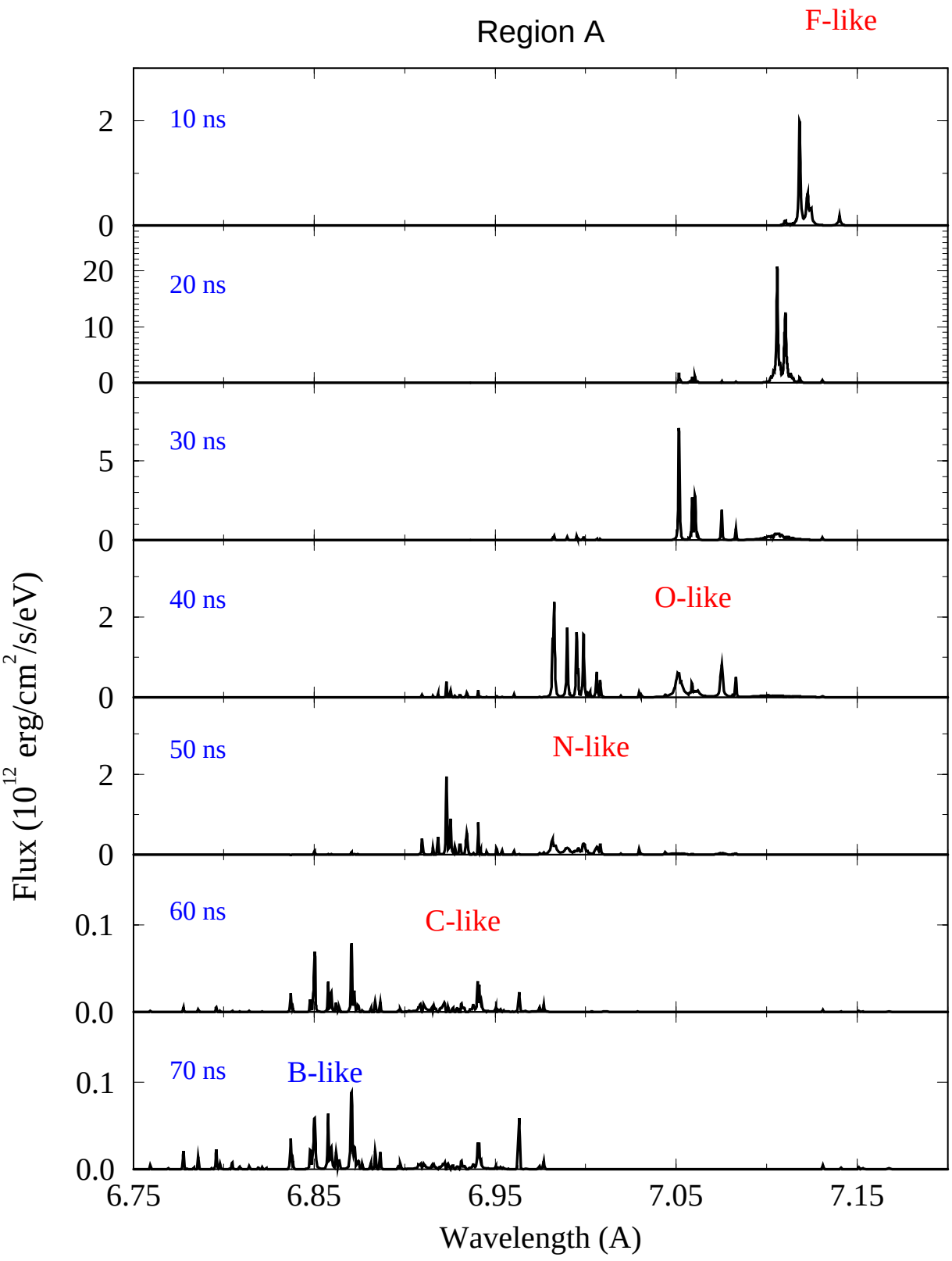

Figure 2.3. Time-dependent K_α emission spectra for Region A of 6 μm-thick Si target.

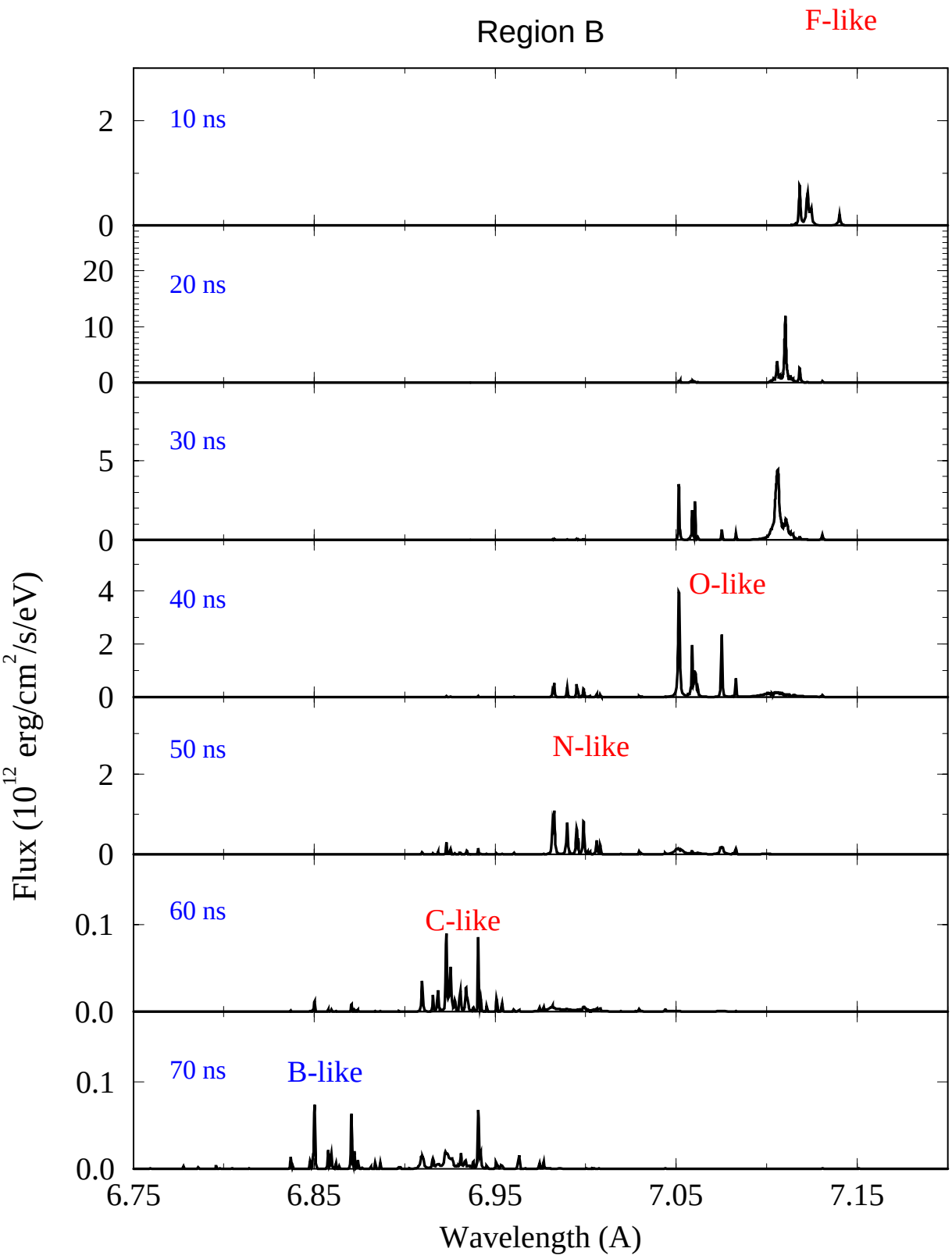

Figure 2.4. Time-dependent K_α emission spectra for Region B of 6 μm-thick Si target.

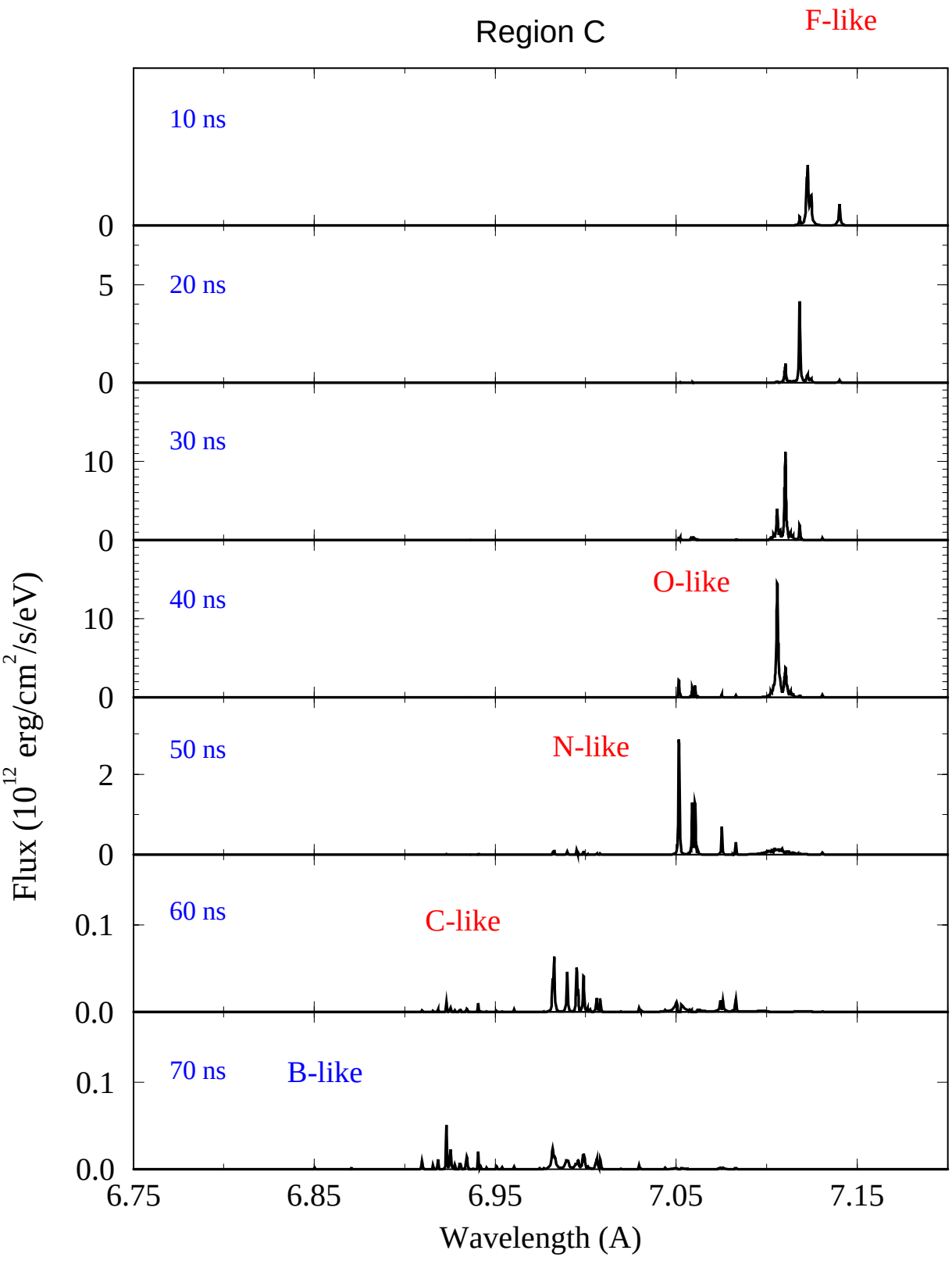

Figure 2.5. Time-dependent K_α emission spectra for Region C of 6 μm-thick Si target.

opacity effects. The reason for the higher intensity of the cold feature is because of the lack of vacancies in the 2p subshell. That is, the lower state of a K_α (1s – 2p) fluorescence transition necessarily has a 2p vacancy. If the surrounding plasma has very few 2p vacancies (due to having $\gtrsim 10$ bound electrons) there is very little opacity. Thus, until the temperature is high enough to ionize the M-shell electrons and begin to excite or ionize L-shell electrons, there is very little K_α line opacity.

Figure 2.5 shows that the peak K_α line flux from Region C occurs at a time of 40 ns, which is substantially later than the peak time of Region A. This occurs, again, because of the low opacity of the low ionization stage K_α lines. In fact, the calculated frequency-integrated K_α flux for Region C at this simulation time is 3.0 times higher than that of Region A. This occurs in spite of the fact that the current density in Region C is a factor of 2.4 times *lower* than Region A. Thus, our simulations predict that a time-resolved x-ray image of this particular target would show a relatively bright ring surrounding a dimmer interior *at this simulation time*.

Figure 2.6 shows the corresponding K_α satellite absorption spectra for Region A for this 6 μm Si target. During the first 20 ns, no absorption features are present between $\lambda = 6.8$ Å and $\lambda = 7.2$ Å. As the plasma heats up, absorption from the K_α transitions of higher and higher ionization stages appears. As pointed out earlier, due to the weakness of the K_α emission lines at late times, absorption spectroscopy may be the best method of characterizing the plasma conditions at late times.

Figures 2.7–2.9 show Si K_α absorption spectra over a wider wavelength range for Regions A, B, and C. The K_α (1s – 2p) lines appear at $\lambda \sim 6.8 - 7.2$ Å. K_β (1s – 3p) absorption lines appear at shorter wavelengths. In these figures, the K_β absorption for each ionization stage appears as a narrow feature. This is simply an artifact of the relatively small number of energy levels included in these calculations which involve K_β transitions. A physically realistic spectrum will include a large number of lines (qualitatively similar to the K_α features). As the plasma heats up, absorption features from higher ionization stages appear.

There are several items worth noting in Figures 2.7–2.9. First, for targets which are a few microns thick, backlighter photons at energies above the bound-free K-edge are predominantly absorbed. When the plasma is cold, this edge appears near $\lambda = 6.66$ Å. As the plasma heats up, the wavelength of this inner-shell photoionization edge shifts significantly to shorter wavelengths. It is important to realize, however, that the edge will not appear as a "clean", isolated edge as shown in these figures. This is because the presence of 1s – 4p,

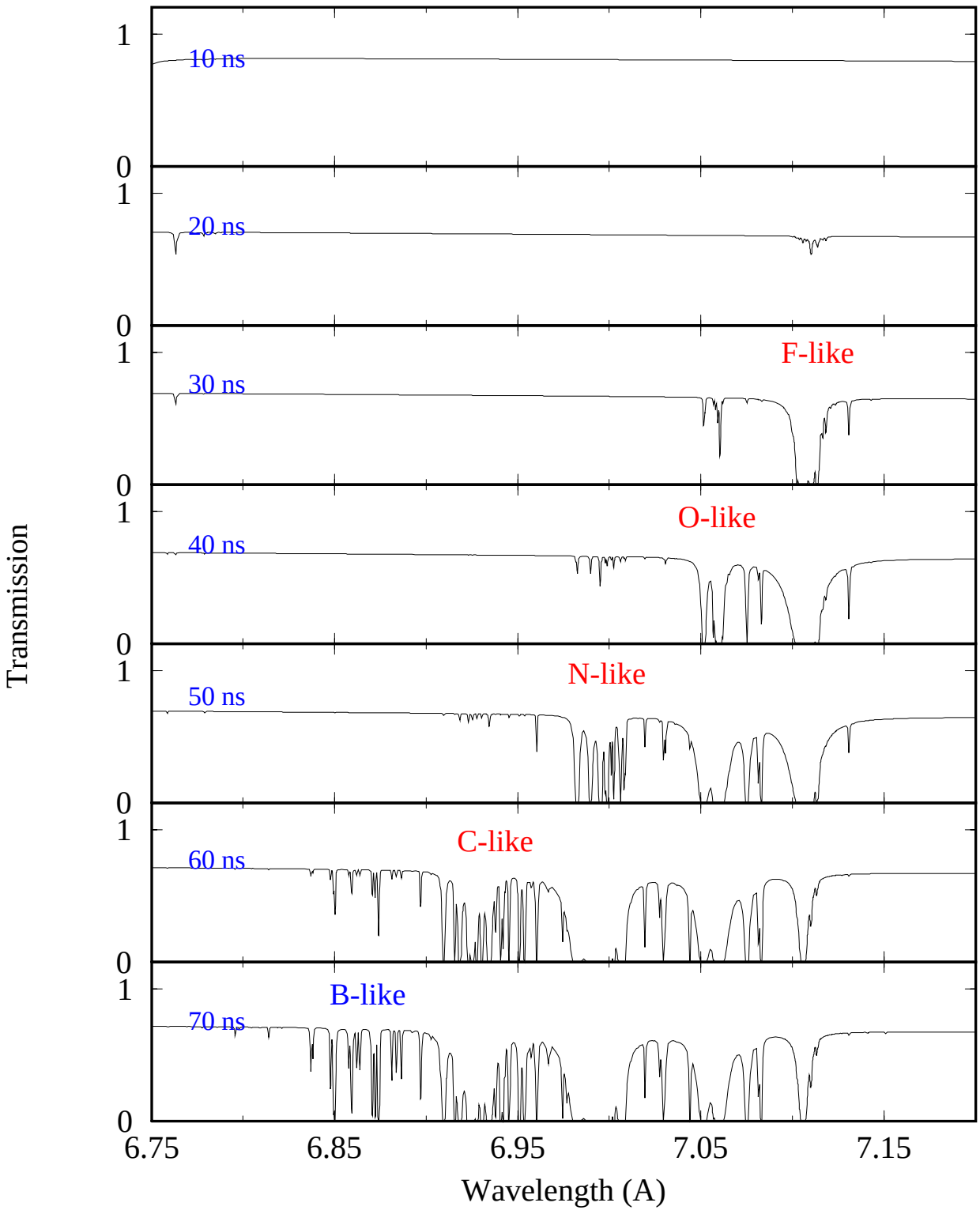

Figure 2.6. Time-dependent K_α absorption spectra for Region A of 6 μm-thick Si target.

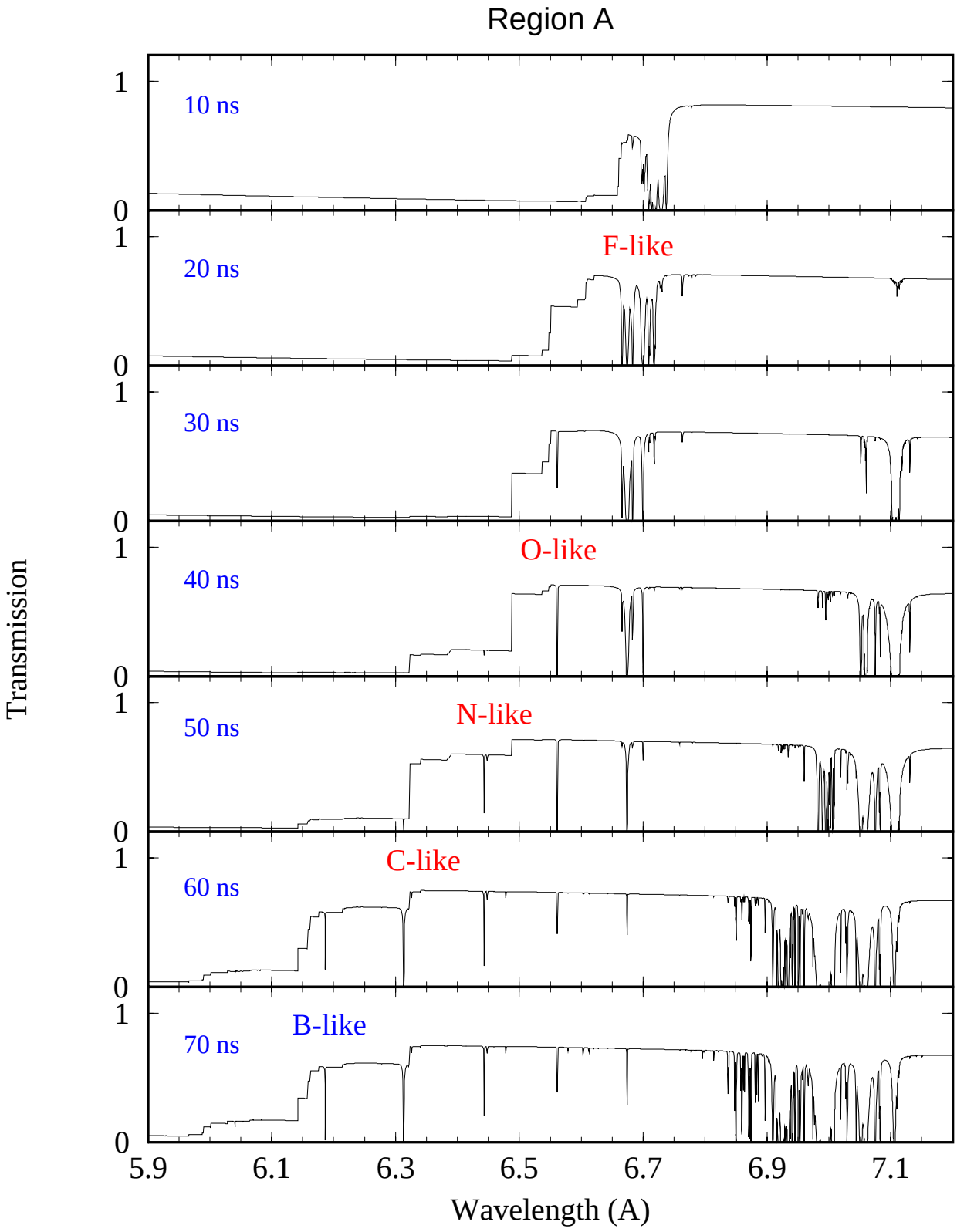

Figure 2.7. Time-dependent K_α and K_β absorption spectra for Region A of 6 μm-thick Si target.

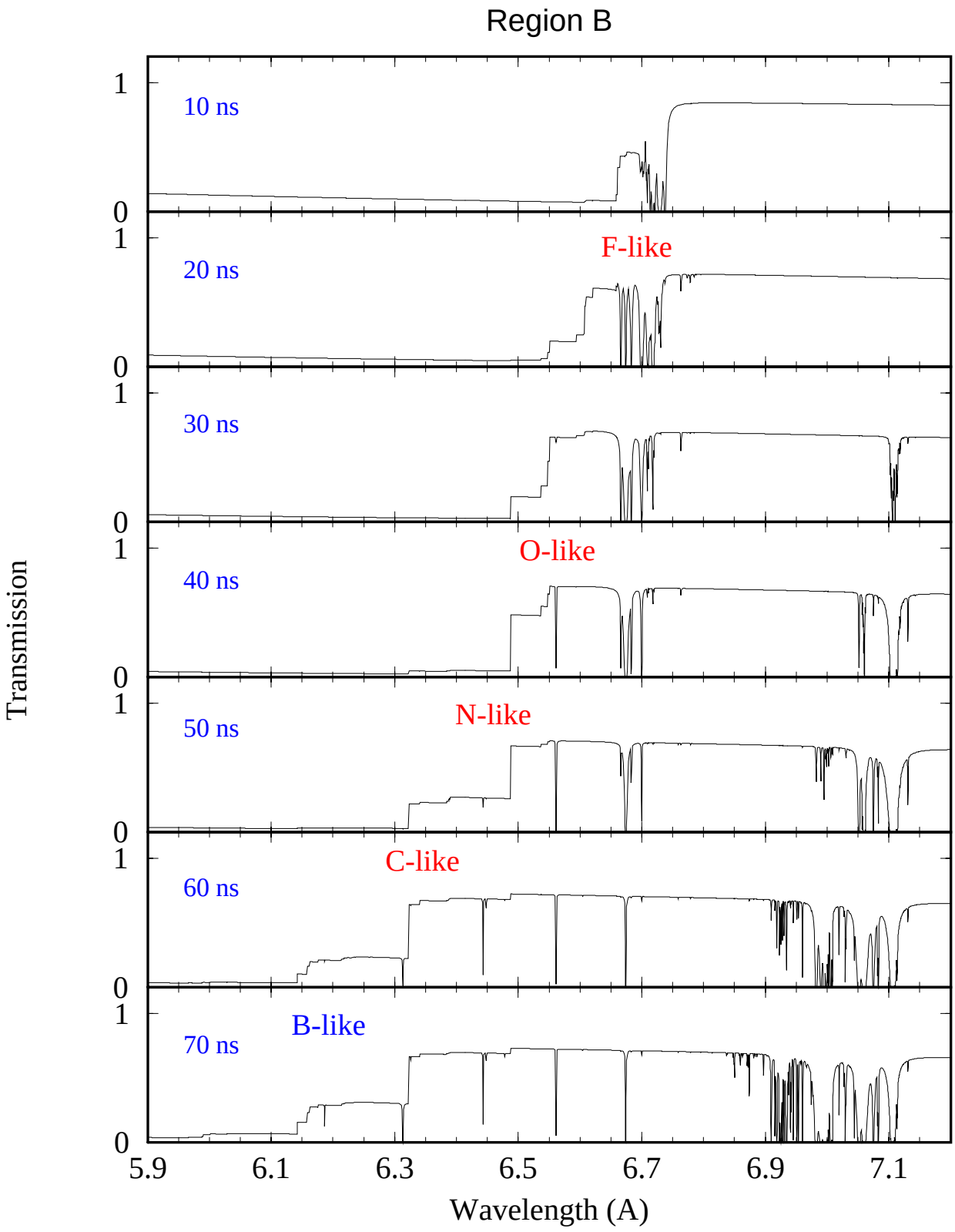

Figure 2.8. Time-dependent K_α and K_β absorption spectra for Region B of 6 μm-thick Si target.

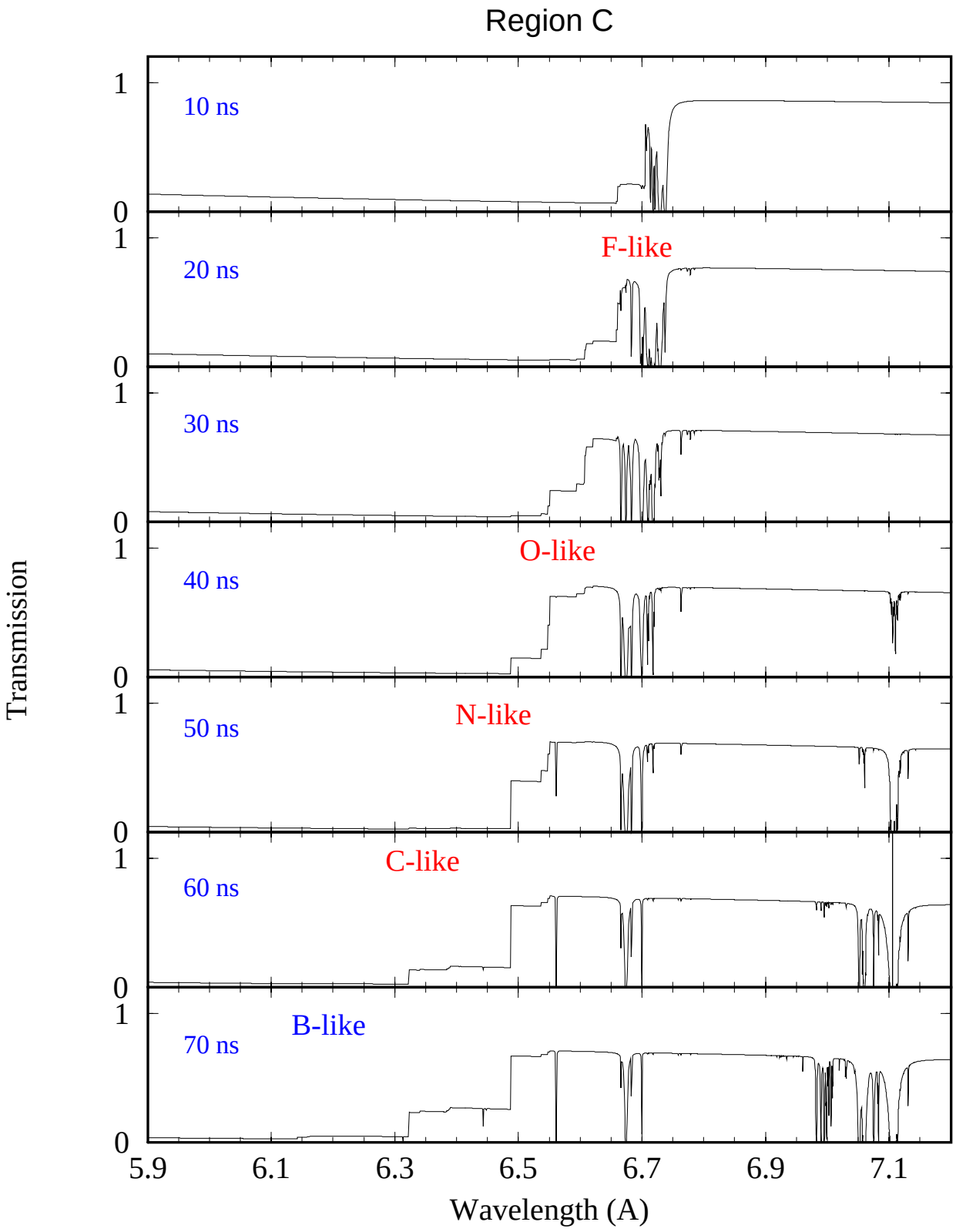

Figure 2.9. Time-dependent K_α and K_β absorption spectra for Region C of 6 μm-thick Si target.

1s – 5p, 1s – 6p, ... transitions should lead to a more continuous increase in the opacity as these transitions "merge" into the photoionization edge. Nevertheless, the large wavelength shift in the K-edge of successively higher ionization stages should provide useful complementary information about the state of the target plasma. This information could be especially valuable in experiments where relatively low spectral resolutions are available.

Figure 2.10 shows the time- and space-integrated K_α emission spectrum for Si. Also shown is the corresponding spectrum for Al (from Ref. [2]). The spectra are qualitatively similar, but there are some important differences. Figure 2.10 shows that the magnitude of the peak K_α flux for Al is about 1.8 times higher than that for Si. The lower Si K_α fluxes are at least in part due to the lower proton-impact ionization cross sections for Si (see Section 2.3). Also note that the flux from the N-like feature of Al is about 3 times higher than that of Si. This is in part due to the fact that, for a given temperature, Al will tend to have fewer bound electrons that Si. We caution, however, that the methodology for setting up the atomic physics cross section files was different for Al and Si. Therefore, the predicted differences in the magnitudes of the Al and Si K_α fluxes must be considered preliminary at this point. The dependence of the total K_α x-ray flux on the target atomic numbers is also discussed in Section 2.3.

2.3. Dependence of Proton Impact Ionization Cross Sections and Fluorescence Yields on Target Atomic Number

Targets composed of sodium, magnesium, aluminum, and silicon ($Z = 11 - 14$) have been considered for K_α spectroscopy beam-target interaction experiments at FZK. In this section, we present results for calculated proton-impact ionization cross sections and fluorescence yields for these elements. The goal is to provide some insights on the dependence of K_α line intensity on atomic number. Although the K_α flux also depends on a number of parameters (the target ionization state, opacity effects, proton beam parameters), it is useful to examine in some detail the beam-impact ionization cross section and fluorescence yield as the intensity of individual K_α lines is proportional to each of these quantities.

To calculate proton impact ionization cross sections, we use a CPSSR model [4], which is a modified plane-wave Born approximation model. Figure 2.11 shows comparisons of our calculated cross sections with experimental data for several cold targets with atomic numbers ranging from 10 to 18. It can be seen that very good agreement is achieved for all targets over a wide range of proton energy.

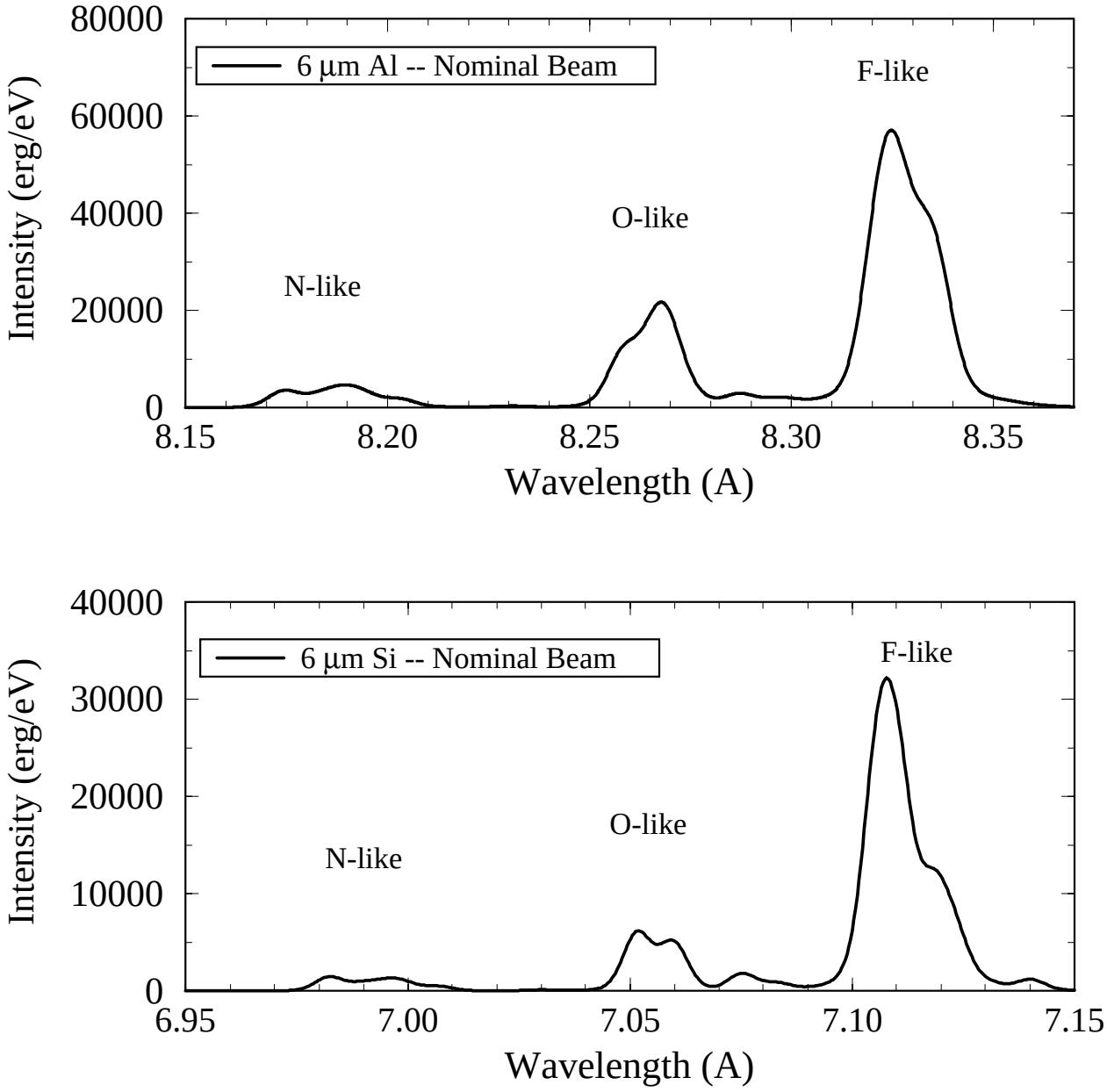

Figure 2.10. Time- and space-integrated K_α emission spectra for a 6 μm Al target (top) and a 6 μm Si target (bottom). These calculated spectra include an instrumental broadening of $\lambda/\Delta\lambda = 1000$.

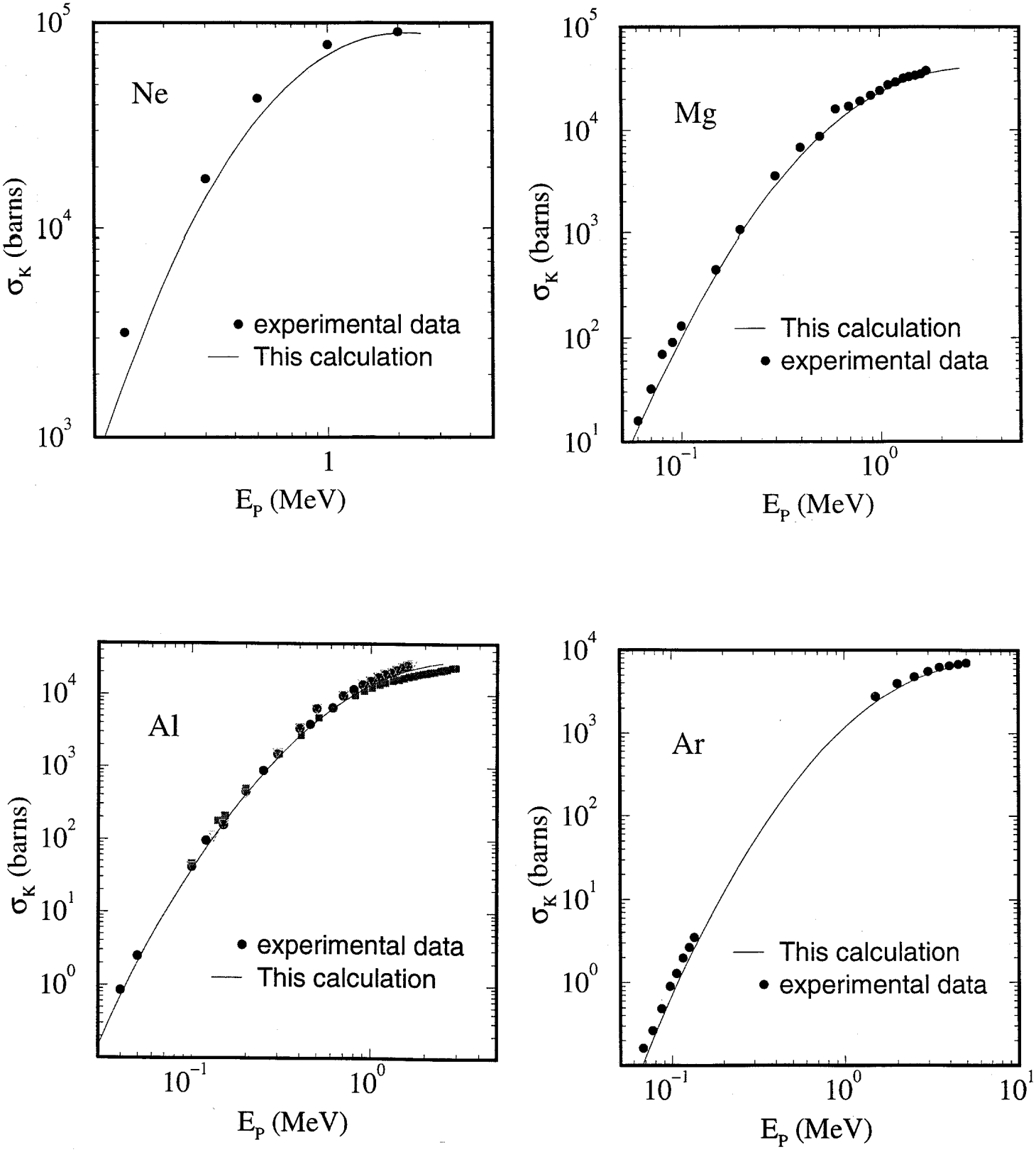

Figure 2.11. Comparison of calculated and experimental proton-impact ionization cross sections for Ne, Mg, Al, and Ar.

In Figure 2.12, we present the single K-shell ionization cross sections as a function of proton energy for the target state $1s^2\ 2s^2\ 2p^6\ 3s^1$ of four different elements: Na, Mg, Al, and Si. In order to see the dependence on ionization state, we also show the corresponding cross section curve of the cold Si (Si I). We can see that at 2.5 MeV, the proton impact ionization cross section for this isoelectronic sequence decreases 40% as the nuclear charge increases by 1, while the decrease is somewhat larger ($\sim 70\%$) for proton energies of 0.5 MeV. This effect can be seen more clearly in the bottom plot of Figure 2.12, where all the cross sections are scaled to the corresponding values of Al.

The effect of target nuclear charge on fluorescence yield is shown in Figure 2.13. It is seen that the fluorescence yield increases as the target nuclear charge increases. Thus, for a given isoelectronic sequence, an increase of the target nuclear charge leads to a decrease in the K-shell ionization cross section and an increase in the fluorescence yield. Note that the x-ray production cross section is proportional to the product of the inner-shell ionization cross section and the corresponding fluorescence yield. Hence, the net change of the x-ray production cross section is less sensitive than that of the K-shell ionization cross section for different target materials. It is important to note, however, that the fluorescence yields of different autoionizing states can be dramatically different ($\sim$ a factor of 2–3 is not uncommon). Thus, the x-ray flux also depends on the ionization/excitation state of the plasma. Figure 2.14 shows our calculated x-ray production cross sections for Na, Mg, Al, and Si. It can be seen that the overall x-ray production cross section decreases as the target nuclear charge Z increases.

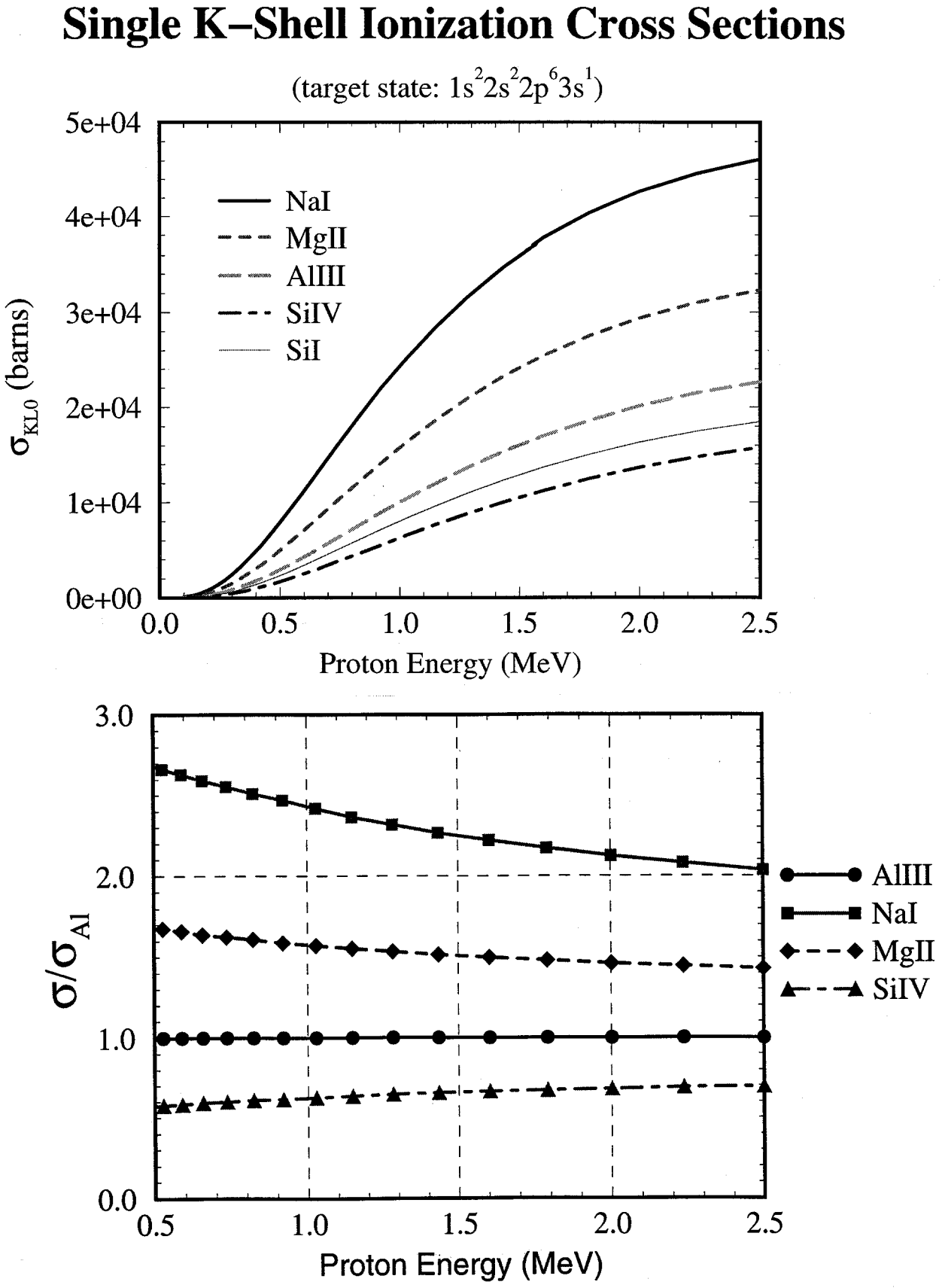

Figure 2.12. (Top) Calculated K-shell proton-impact ionization cross sections for Na I, Mg II, Al III, Si IV. In each case the target state configuration is $1s^2\ 2s^2\ 2p^6\ 3s^1$. (Bottom) Same cross sections scaled to σ_K (Al III) = 1.

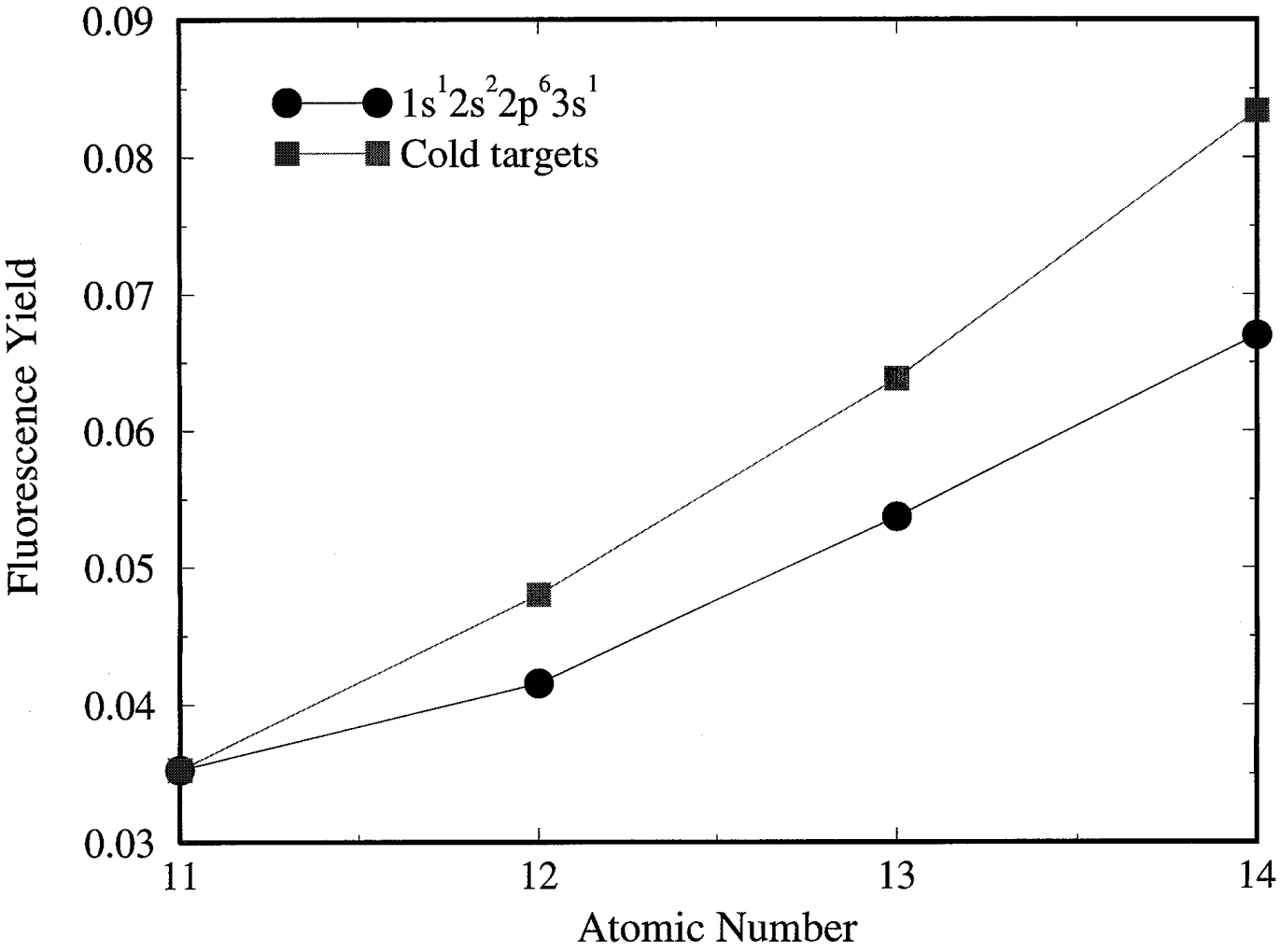

Figure 2.13. Calculated fluorescence yield as a function of atomic number for $1s^2\ 2s^2\ 2p^6\ 3s^1$ isoelectronic sequence (top curve with squares) and cold (i.e., neutral) atoms (bottom curve).

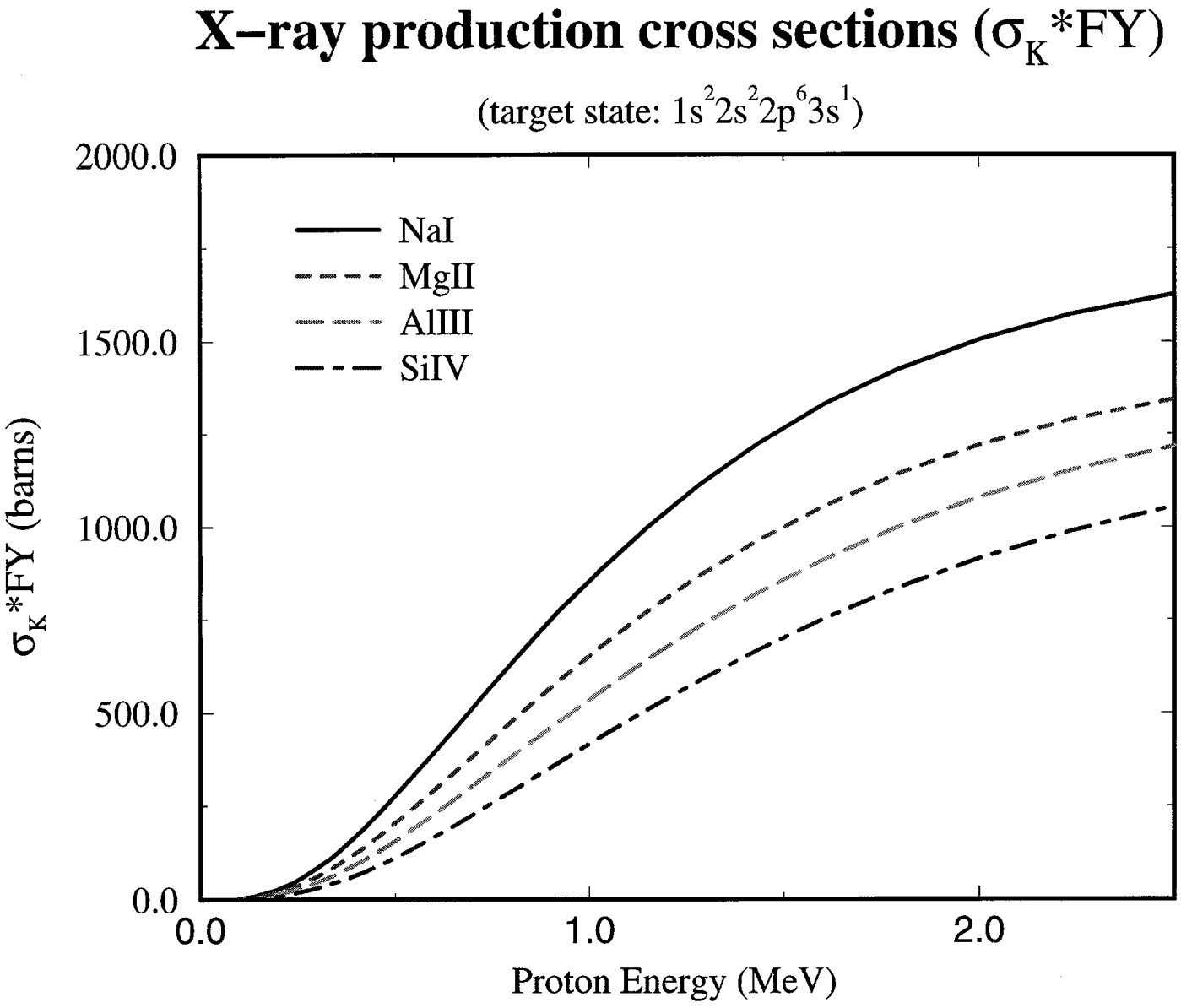

Figure 2.14. X-ray production cross sections for $1s^2$ $2s^2$ $2p^6$ $3s^1$ isoelectronic sequence.

3. Improvements to Collisional-Radiative Modeling

During the past year, we have made several improvements to our collisional-radiative spectral analysis code NLTERT. These include (1) modifying the solution of the multilevel atomic rate equations to allow for a time-dependent solution; and (2) including a continuum lowering model based on the occupation probability formalism of Hummer and Mihalas [1]. In this section we provide a description of these models, some sample results, and a description of how they are implemented in NLTERT.

3.1. Time-dependent Collisional-Radiative Model

For experiments involving low-to-moderate density plasmas, the plasma conditions can sometimes change on time scales which are fast compared to the "relaxation" times of various collisional and radiative processes. In such situations, an accurate calculation of the atomic level populations requires the solution of *time-dependent* atomic rate equations. For a multilevel system, the atomic rate equations can be written as:

$$\frac{dn_i}{dt} = n_i \sum_{j \neq i}^{N_L} W_{ij} + \sum_{j \neq i}^{N_L} n_j W_{Ji} \,, \qquad (i = 1,\, N_L) \tag{3.1}$$

where n_i is the population of atomic level i, W_{ij} and W_{ji} are the depopulating and populating rates of level i due to level j, and N_L is the total number of levels in the system. For upward transitions ($i < j$),

$$\begin{aligned} W_{ij} &= B_{ij}\,\bar{J}_{ij} + n_e\,C_{ij} + \\ &+ \beta_{ij} + n_e\,\gamma_{ij} + \mathcal{R}_{ij}^{\rm ion} + \mathcal{R}_{ij}^{{\rm hot}\,e} \,, \end{aligned} \tag{3.2}$$

while for downward transitions,

$$\begin{aligned} W_{ji} &= A_{ji} + B_{ji}\,\bar{J}_{ji} + n_e\,D_{ji} + \\ &+ n_e\,(\alpha_{ji}^{RR} + \alpha_{ji}^{DR}) + n_e^2\,\delta_{ji} + \Omega_{ji} \,, \end{aligned} \tag{3.3}$$

where n_e is the electron density and $\bar{J}_{ij}\,(\equiv \int \phi_{ij}(\nu)\,J_\nu\,d_\nu)$ is the frequency-averaged mean intensity of the radiation field for a bound-bound transition. The rate coefficients in the above equations are:

$$\begin{aligned} A_{ij} &= \text{spontaneous emission} \\ B_{ij} &= \text{stimulated absorption } (i < j) \text{ or emission } (i > j) \end{aligned}$$

$$
\begin{aligned}
C_{ij} &= \text{collisional excitation} \\
D_{ij} &= \text{collisional deexcitation} \\
\alpha_{ij}^{RR} &= \text{radiative recombination} \\
\alpha_{ij}^{DR} &= \text{dielectronic recombination} \\
\beta_{ij} &= \text{photoionization plus stimulated recombination} \\
\gamma_{ij} &= \text{collisional ionization} \\
\delta_{ij} &= \text{collisional recombination} \\
\mathcal{R}_{ij}^{\text{ion}} &= \text{ion beam impact ionization/excitation} \\
\Omega_{ij} &= \text{autoionization} \\
\mathcal{R}_{ij}^{\text{hot } e} &= \text{hot (non-Maxwellian) electron ionization/excitation.}
\end{aligned}
$$

Note that NLTERT now has the capability to also model non-Maxwellian electron distributions, which is relevant to problems in which a "hot" electron component can affect spectra.

Previously in NLTERT, collisional-radiative *equilibrium* (CRE) was assumed, and the LHS of Eq. (3.1) was set to zero. In this case, the n_i are simultaneously determined by inverting a matrix using LAPACK [6]. When CRE is not assumed, one must solve a coupled set of ordinary differential equations (ODE's). To do this, we utilize the LSODE package [7]. Examples of the use of the time-dependent option are given in Section 3.3.

3.2. Pressure Ionization Modeling with Occupation Probability Formalism

A significant difference between atomic structure for isolated atoms and those in the plasma is the finite number of bound states in the latter case. As the plasma density rises and the number and intensity of interparticle interactions increases, less tightly bound states are strongly perturbed, broadened into distributions resembling conduction bands, and ultimately destroyed and shifted into the continuum. These phenomena imply a *pressure ionization* which leads at very high densities to a fully ionized plasma comprising, in the first approximation, an ideal gas of degenerate electrons that can move freely with respect to a "lattice" of bare ions. Pressure ionization is primarily a volume effect: when particles are jammed closely together, bound electron orbitals filling too large a volume fail to survive and the electrons migrate from atom to atom.

The destruction of excited (unoccupied) levels with high quantum numbers affects the plasma emission or absorption opacity. At very high densities, pressure begins to release electrons from occupied core levels. This increases the average ionization state and changes the plasma energy, pressure, and transport coefficients.

During the past several decades, many different pressure ionization models have been developed [8–11]. A summary of various pressure ionization models is presented in Ref. [12]. A procedure for modeling pressure ionization has recently been suggested by Hummer and Mihalas [1] called the "occupation probability formalism". In this procedure, a factor, w_{ijk} ($0 \leq w_{ijk} \leq 1$), is introduced for each atomic level. The physical significance of w_{ijk} is that it is the probability of finding the ion in question in state i relative to that of finding it in a similar ensemble of non-interacting ions. Alternatively, w_{ijk} can be considered as a factor expressing the survival probability of the level due to the perturbation of surrounding particles, neutral and charged. The *survival probability* has to be calculated directly from a physical description of interparticle interactions. It is here that one makes contact with atomic physics and can attempt to introduce some level of realism into the model.

In the model suggested by Hummer and Mihalas, perturbations by neutral particles are based on an excluded volume treatment, and perturbations by charged particles are calculated from a fit to a quantum mechanical Stark ionization theory. The level survival probability of level i of ion j of species k can then be expressed as [1]:

$$w_{ijk} = \int_0^{\beta_{ijk}} d\beta P_H(\beta) \equiv Q(\beta_{ijk}), \tag{3.4}$$

where

$$P_H(\beta) = (2\beta/\pi) \int_0^{\infty} dy \, \exp(-y^{3/2}) \, y \, \sin(\beta y) \tag{3.5}$$

is the Holtsmark distribution function. The numerical calculation of the Holtsmark distribution $P(\beta)$ and its cumulative $Q(\beta)$ can be accomplished with the scheme developed by Hummer [13]. The critical value of β is a function of plasma conditions and can be written as:

$$\beta_{ijk} = \frac{K_{ijk}(I_{ijk}^2/4Z_{jk})(4\pi a_0^3/3)^{-2/3} N_{ion}^{1/3}}{N_e} \, . \tag{3.6}$$

An alternative, but more computationally efficient, approximate expression of w_{ijk} is:

$$\ln\, w_{ijk} \;=\; -\left(\frac{4\pi}{3}\right)\left\{\sum_{\nu' k'} n_{\nu' k'}\left[(r_{ijk}+r_{1\nu' k'})^3+\beta(r_{1jk}+r_{1\nu' k'})^\gamma\right]\right.$$

$$\left. +\;\; 16\left[\frac{\sqrt{z_{jk}+1}\; e^2}{\sqrt{K_{ijk}}\; I_{ijk}}\right]^3 \sum_{s\neq e} n_s z_s^{3/2}\right\}. \tag{3.7}$$

Here the index ν' runs over neutral particles, $n_{\nu' k'}$ is the number density of neutral particle of species k', r_{ijk} is the radius assigned to a particle in state i of ion j of species k, I_{ijk} is the ionization potential of such a particle, z_{jk} is the net charge of a particle of ion j of species k, β and γ are two empirical parameters, and n_s is the number density of the charged ion. Z_s is the net charge of the ion, s runs over all charged particles except for electrons, and

$$K_{ijk} = \begin{cases} 1 & p_i \leq 3 \\ \dfrac{16}{3}\left(\dfrac{p_i}{p_i+1}\right)^2 \dfrac{p_i+7/6}{p_i^2+p_i+1/2} & p_i > 3 \end{cases} \tag{3.8}$$

is a quantum mechanical correction and p_i is the effective quantum number of the state i.

The occupation probability formalism has several advantages. First, the w_{ijk} decrease continuously and monotonically as the strength of the relevant interaction increases relative to the binding energy of a level. Second, the continuous state-by-state fadeout with decreasing w_{ijk} allows one to assure continuity of all material properties (pressure, internal energy, opacity, etc.). Finally, the probabilistic interpretation of w_{ijk} allows one to combine survival probabilities from statistically independent interactions. It is thus straightforward to allow for the simultaneous action of different mechanisms, as well as of several different species of perturbers by any one mechanism. Thus, the method provides a scheme for treating partially ionized plasmas, and it goes smoothly to the limits of completely neutral or completely ionized gas.

3.3. Implementation of Time-Dependent Collisional-Radiative and Pressure Ionization Models in NLTERT

Next, we give two examples of a time-dependent collisional-radiative model. Both cases are test problems from the Non-LTE Kinetics Workshop, which took place in Gaithersburg, MD, in August 1996. The first case involves an Ar tracer in an imploding hydrogen plasma, which is relevant to present-day ICF capsule implosion experiments. The

second involves a recombining carbon plasma, which is motivated by short pulse laser experiments.

Figure 3.1 shows the input file for the first example. Input to the problem includes the time dependent electron density and temperature, which are shown in Figure 3.2. Here, it is seen that a slow increase in the electron density and temperature occurs until about 1.2 ns, at which time both increase very abruptly. The purpose of the simulation is to track the time-dependent ionization dynamics of the Ar tracer.

In the input file for this simulation, integer switch ISW(1) = 1 specifies that this is a time-dependent collisional-radiative simulation. The variables ISW(11), NTIMES, DELTAT, and TIMEND are used to set up the simulation time grid and end time. At each point in this time grid the rate coefficients are updated and the multilevel atomic rate equations are solved to get new atomic level populations. The time-dependent electron temperature and density in this simulation are not supplied in the NAMELIST input file, but are read in from a file named 'TimeDep.Plasma.vs.t'. This file is read by subroutine RDPLAS. The time grid in the plasma specification file and the simulation time grid are generally different. A time-interpolation is performed to get T_e and n_e at the appropriate simulation time.

Figure 3.3 shows results for the mean charge state, $\bar{Z}$, as a function of time. Here, it is seen $\bar{Z}$ rises slowly up to a value of 6.5, and then rapidly increases to $\bar{Z} \approx 15.5$ at 1.2 ns, which is the time when n_e and T_e increase dramatically.

Figure 3.4 shows the input file for the time-dependent collisional-radiative simulation of the recombining carbon plasma. In this case, the electron temperature and ion density are constant in time (ISW(41) = 0, TEMPEL = 2 eV, DENSNN = 10^{19} ions/cm^3). The carbon is initially fully ionized (ISELCT = 2 for that level, and ISW(6) = -1). A simulation time grid is set up which is uniformly spaced logarithmically in time. The initial time is TCRMIN = 10^{-16} s, the final time is TCRMAX = 10^{-8} s.

In this simulation, the continuum lowering model is set as follows. ICONTL is used to specify whether the occupation probability model is to be utilized and whether the ionization threshhold is to be adjusted downward (continuum lowering). The switch ISW(51) specifies whether the exact formula for the occupation probability, w_{ijk} in Eq. (3.5), is to be used, or whether the approximate formulation (Eq. (3.8)) is utilized. Note that by setting ISW (51) = $n_{\max}$, a discrete cutoff in the principal quantum number is performed. That is, $w_n = 1$ for $n \leq n_{\max}$ and $w_n = 0$ if $n > n_{\max}$.

```
 $input1
c ...                   TIME STEPPING parameters
c                         if isw1 =  0 => steady-state calculation
c                         if isw1 <> 0 => time-dependent calculation
    isw(1) = 1
c                         there should be NTIMES+1 values for TIMSIM
c                         if isw11=0 => specify times
c                         if isw11=1 => uniform times given by "deltat"
c                         if isw11=2 => uniform log-spaced times given
c                                       by tcrmin, tcrmax
    isw(11) = 1
    ntimes = 300
    deltat = 0.02e-9
    timend = 2.e-9
c
    rtolls = 1.e-4
    atolls = 1.e-12
    mfls   = 21
c
c ...                   if isw42<>0, hold electron density constant
    isw(42) = 0
c ...                   Photoexcitation/photoioniz. (skip if isw7,isw8<>0)
    isw(7) = 1, 1
c ...                   CONTINUUM LOWERING PARAMETERS
c                         if icontl=0 => compute occ prob & cont lowering
c                         if icontl=1 => compute occ prob only
c                         if icontl=2 => compute cont lowering only
c                         if icontl<0 => compute neither
    icontl = 0
c                         if isw51=0 => use Hummer approx formula for w_n
c                         if isw51=1 => use Hummer exact formula for w_n
c                 t       if isw51<0 => use nprin_max = -isw51
    isw(51) = 0
c                         con(60) defines continuum lowering delta-E
c                                 [1st level where ocprob < con60]
    con(60) = 0.1
c                         if isw60=0, set dE of all levels of same ion
c                                     to declow(iupper)
    isw(60) = 0
c ...                   STARTING POPULATIONS
c                         isw6=-1=> pop's are user specified with iselct=2
c                         isw6=1 => LTE populations at T=TEMPIN
c                         isw6=2 => CRE/thin populations at T=TEMPIN
    isw(6) = -1
c ...                   GRID and THERMO PARAMETERS
    igeom = 1
    nzones = 1    e
c ...                     Zoning switches
    isw(15) = 0
    isw(44) = 0
c
    radmin = 0.
    radmax = 1.6e-7
    dradmn = 1.6e-8
c ...                     if isw41=0 => use constant (input) thermo props
c                         if isw41=1 => read in time-dependent plasma
c                                       conditions from
    isw(41) = 1
c                         con91 = min T_e allowed
    con(91) = 1.
c ...                   ATOMIC DATA parameters
     ngases = 1
     ilinep = 3
c Ar
     ireada(1) = 1
     atomnm(1) = 18.
     atomwt(1) = 40.
c                       ======================
c ...                   SELECT LEVELS FOR ARGON
c                       ======================
c
c  Ar I       Ar-like
     iselct(   1,1)  = 2, 10*1
c  Ar II      Cl-like
     iselct(  33,1)  = 10*1
c  Ar III     S-like
     iselct( 100,1)  = 10*1
c  Ar IV      P-like
     iselct( 170,1)  = 10*1
c  Ar V       Si-like
     iselct( 240,1)  = 10*1
c  Ar VI      Al-like
     iselct( 276,1)  = 10*1
c  Ar VII     Mg-like
     iselct( 311,1)  = 10*1
c  Ar VIII    Na-like
     iselct( 347,1)  = 10*1
c  Ar IX      Ne-like
     iselct( 384,1)  = 10*1
c  Ar X       F-like
     iselct( 417,1)  = 10*1
c  Ar XI      O-like
     iselct( 556,1)  = 10*1
c  Ar XII     N-like
     iselct( 761,1)  = 10*1
c  Ar XIII    C-like
     iselct( 942,1)  = 10*1
c  Ar XIV     B-like
     iselct(1084,1)  = 10*1
c  Ar XV      Be-like
     iselct(1187,1)  = 10*1
c  Ar XVI     Li-like
     iselct(1318,1)  = 24*1
c  Ar XVII    He-like
     iselct(1384,1)  = 34*1
c  Ar XVIII   H-like
     iselct(1434,1)  = 10*1
c  Ar XIX     Fully ionized
     iselct(1454,1)  = 1
c
 $end
```

Figure 3.1. Input file for time-dependen collisional-radiativ simulation of Ar-doped imploding capsule.

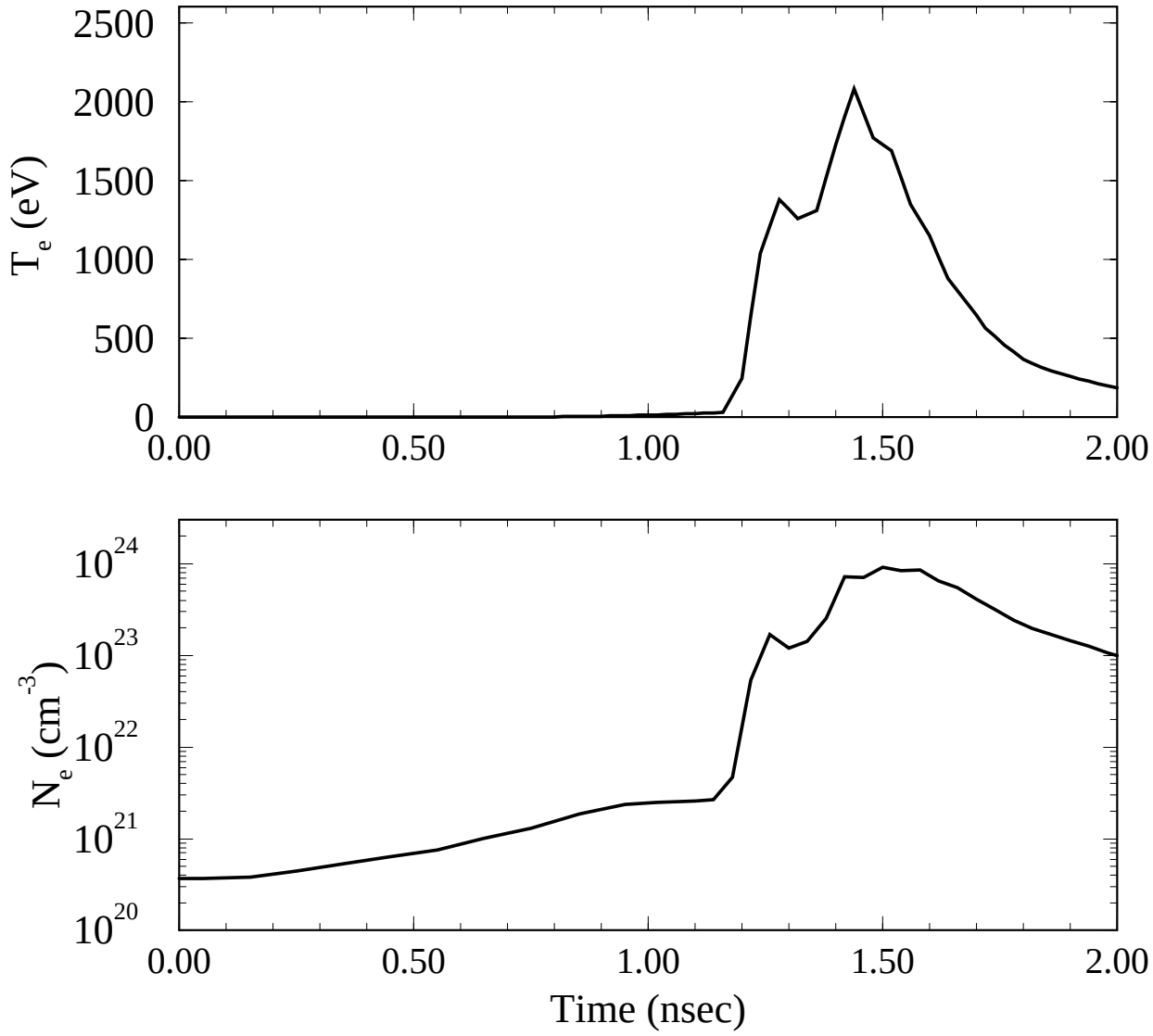

Figure 3.1. User-specified time-dependent electron density and temperature for Ar-doped imploding capsule simulation.

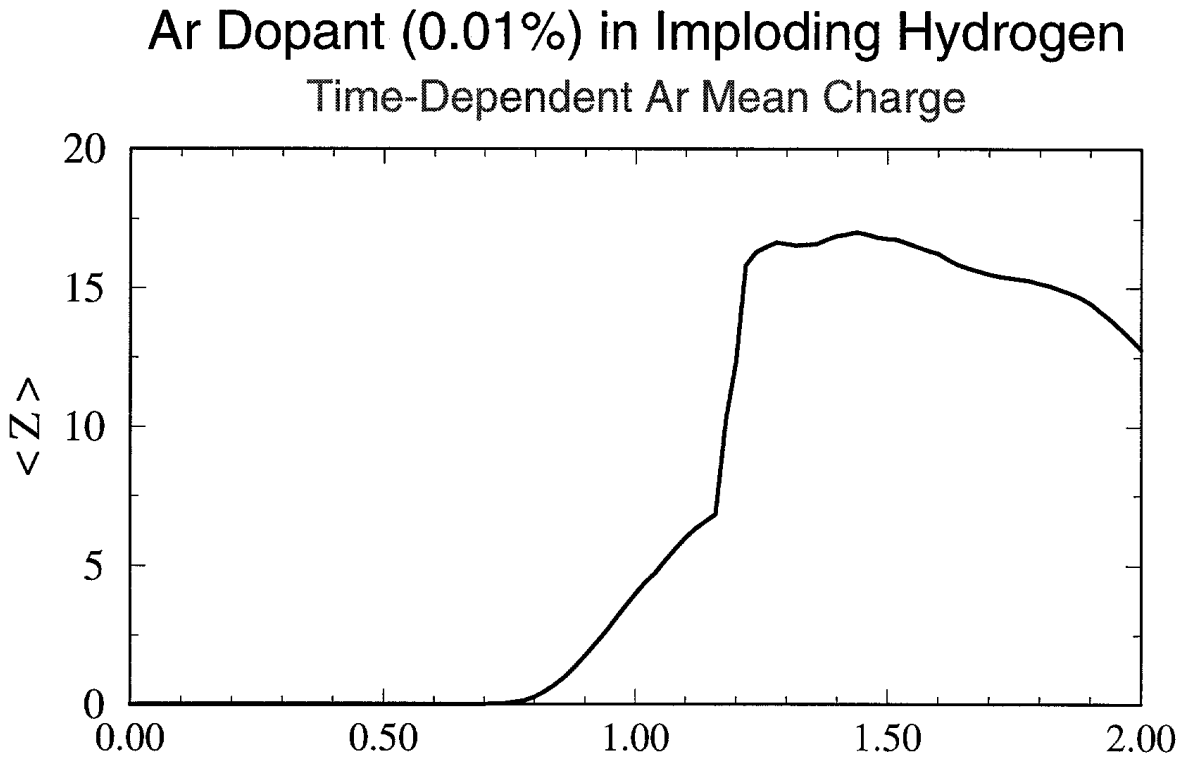

Figure 3.2. Evolution of Ar mean charge state for Ar-doped imploding capsule simulation.

```
 $input1
c ...                   TIME STEPPING parameters
c                         if isw1 =  0 => steady-state calculation
c                         if isw1 <> 0 => time-dependent calculation
   isw(1) = 1
c                         there should be NTIMES+1 values for TIMSIM
c                         if isw11=0 => specify times via "timsim" array
c                         if isw11=1 => uniform times given by "deltat"
c                         if isw11=2 => uniform log-spaced times given
c                                       by tcrmin, tcrmax
   isw(11) = 2
   ntimes = 20
   tcrmin = 1.e-16
   tcrmax = 1.e-8
   timend = 1.01e-8
c
c  timsim(1) = 0., 1.e-15, 1.e-14, 1.e-13, 1.e-12, 1.e-11, 1.e-10,
c
   rtolls = 1.e-4
   atolls = 1.e-12
   mfls   = 21
c
c ...                     if isw42<>0, hold electron density constant
   isw(42) = 0
c ...                     Photoexcitation/photoioniz. (skip if isw7,isw8<>
0)
   isw(7) = 1, 1
c ...                   CONTINUUM LOWERING PARAMETERS
c                         if icontl=0 => compute occ prob & cont lowering
c                         if icontl=1 => compute occ prob only
c                         if icontl=2 => compute cont lowering only
c                         if icontl<0 => compute neither
   icontl = 0
c                         if isw51=0 => use Hummer approx formula for w_n
c                         if isw51=1 => use Hummer exact formula for w_n
c                         if isw51<0 => use nprin_max = -isw51
   isw(51) = 0
c  isw(51) = -6
c                         con(60) defines continuum lowering delta-E
c                                 [1st level where ocprob < con60]
   con(60) = 0.1
c                         if isw60=0, set dE of all levels of same ion
c                                     to declow(iupper)
   isw(60) = 0
c ...                   STARTING POPULATIONS
c                         isw6=-1=> pop's are user specified with iselct=2
c                         isw6=1 => LTE populations at T=TEMPIN
c                         isw6=2 => CRE/thin populations at T=TEMPIN
   isw(6) = -1
c ...                   GRID and THERMO PARAMETERS
   igeom = 1
   nzones = 1
c ...                     Zoning switches
   isw(15) = 0
   isw(44) = 0
c
   radmin = 0.
   radmax = 1.6e-7
   dradmn = 1.6e-8
c ...                     if isw41=0 => use constant (input) thermo props
c                         if isw41=1 => read in time-dependent plasma
c                                       conditions from
    isw(41) = 0
c                         Specify Temperature and Ion Density
   tempel(1) = 1*2.
   densnn(1) = 1*1.e19
```

```
c ...                     ATOMIC DATA PARAMETERS
   ngases = 1
   ilinep = 3
c Carbon
   ireada(1) = 1
   atomnm(1) = 6.
   atomwt(1) = 12.
c                         ========================
c ...                     SELECT LEVELS FOR CARBON
c                         ========================
c  C I
      iselct(  1,1)  = 0
c  C II
      iselct(142,1)  = 1
c  C III
      iselct(245,1)  = 63*1
c  C IV
      iselct(376,1)  = 33*1
c  C V
      iselct(442,1)  = 43*1
c  C VI
      iselct(492,1)  = 20*1
c  C VII
      iselct(512,1)  = 2
 $end
```

Figure 3.4. Input file for time-dependen collisional-radiative simulation of carbon recombination problem.

Figure 3.5 shows the time-dependent mean ionization state of the recombining carbon. Results are shown for 4 cases. The solid curve represents the case in which the occupation probability model was used. Also shown are 3 results in which a user-specified cutoff in the principal quantum number, $n_{\max}$, is utilized. It is seen that the early-time recombination is very sensitive to $n_{\max}$. This is due to the fact that collisional (3-body) recombination into high-n states dominates the recombination process. If more high-n states are available for recombining, the rate is enhanced. Note that the occupation probability model gives an effective $n_{\max}$ of $\sim$ 7 to 8 (in this case, the dissolution of high-n states is continuous). Plottable results for the mean charge are written to the file 'zbar.vs.time'.

Acknowledgement

Support for this work has been provided by Forschungszentrum Karlsruhe, through Fusion Power Associates.

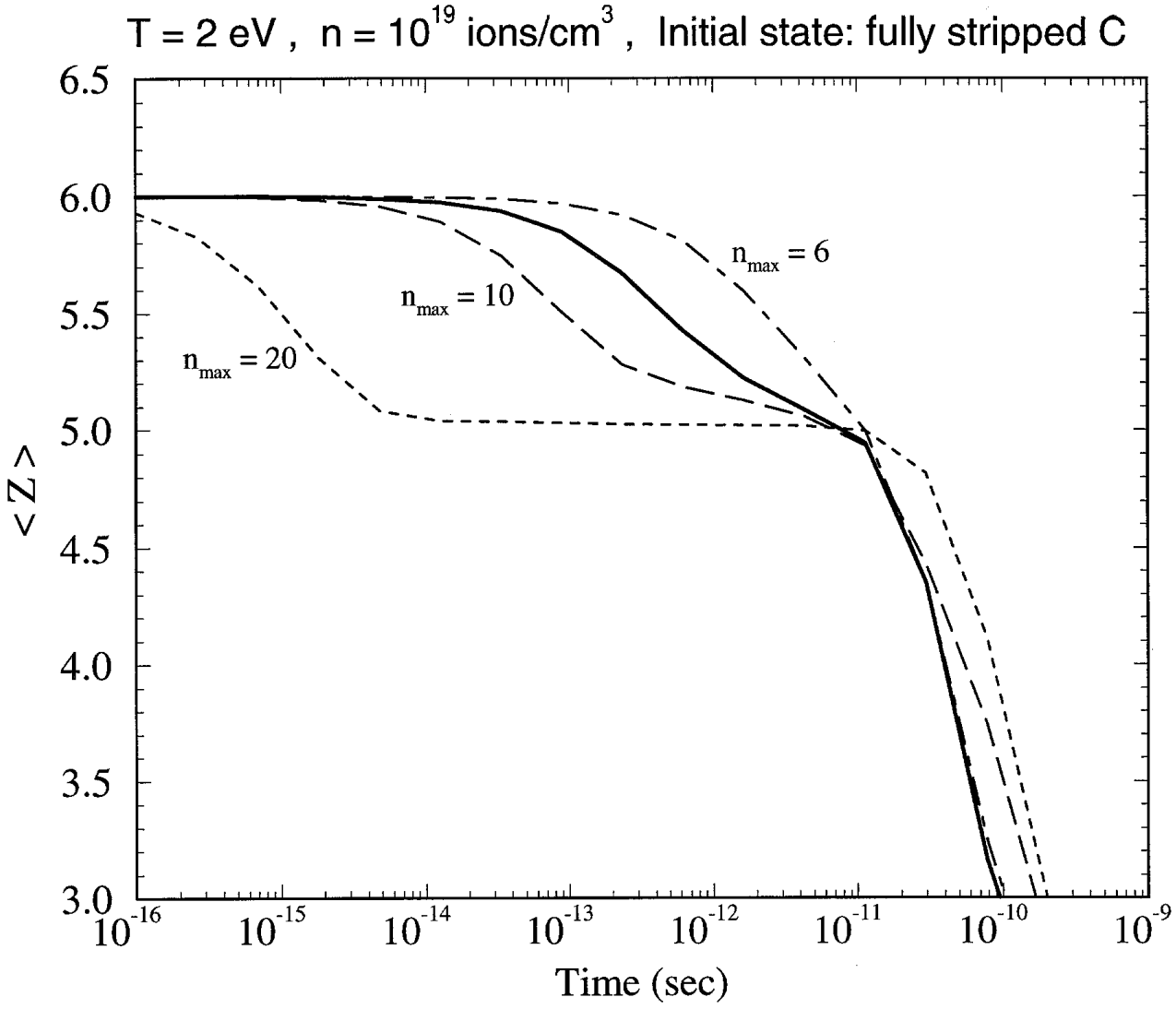

Figure 3.3. Evolution of mean charge state for carbon recombination problem. Solid curve: occupation probability model. Other curves indicate assumed maximum principal quantum number.

References

1. D. G. Hummer and D. Mihalas, *Astrophys. J.* **331**, 794 (1988).

2. J. J. MacFarlane and P. Wang, "Preliminary Analysis of Aluminum K_α Satellite Spectra Obtained in KALIF Applied-B Diode Experiments," Fusion Power Associates Report FPA-96-3 (July 1996).

3. J. J. MacFarlane, G. A. Moses, and R. R. Peterson, "BUCKY-1 – A 1-D Radiation-Hydrodynamics Code for Simulating Inertial Confinement Fusion High Energy Density Plasmas," University of Wisconsin Fusion Technology Institute Report UWFDM-984 (August 1995).

4. P. Wang, J. J. MacFarlane, and G. A. Moses, *Laser and Particle Beams* **13**, 191 (1995).

5. J. J. MacFarlane, "NLTERT – A Code for Computing the Radiative Properties of Non-LTE Plasmas," Fusion Power Associates Report FPA-93-6 (December 1993).

6. E. Anderson et al., LAPACK Users' Guide (SIAM, Philadelphia, 1992).

7. A. C. Hindmarsh, "LSODE and LSODI, Two New Initial Value Ordinary Differential Equations Solvers," ACM SIG NUM Newsletter, Vol. 15, No. 4, 10 (1980).

8. R. M. More, *JQSRT* **27**, 345 (1982).

9. A. Vinogradov, I. Sobelman, and E. Yukov, *Sov. J. Quantum Electron.* **4**, 149 (1974).

10. S. Brush, H. Sahlin and E. Teller, *J. Chem Phys.* **45**, 2102 (1966).

11. H. R. Griem, *Plasma Spectroscopy*, McGraw-Hill, New York (1964).

12. R. M. More, in *Atoms In Unusual Situations*, edited by J. P. Briand, Plenum Publishing Corporation (1986).

13. D. G. Hummer, *JQSRT* **36**, 1 (1986).